Applied Geochemistry 162 (2024) 105904

Contents lists available at ScienceDirect

Applied Geochemistry

journal homepage: www.elsevier.com/locate/apgeochem

Efficient chemical and microbial removal of iron and manganese in a rapid sand filter and impact of regular backwash

Signe Haukelidsaeter [a,*], Alje S. Boersma [b], Lina Piso [a,b], Wytze K. Lenstra [a,b], Niels A.G.M. van Helmond [a,b], Frank Schoonenberg [c], Erik van der Pol [c], Luis C.C. Hurtarte [d,e], Paul W.J.J. van der Wielen [f,g], Thilo Behrends [a], Maartje A.H.J. van Kessel [b], Sebastian Lücker [b], Caroline P. Slomp [a,b]

[a] Department of Earth Sciences, Faculty of Geosciences, Utrecht University, P.O Box 80021, 3508 TA, Utrecht, the Netherlands
[b] Department of Microbiology, Radboud Institute of Biological and Environmental Science, Faculty of Science, Radboud University, P.O. Box 9010, 6500 GL, Nijmegen, the Netherlands
[c] Vitens N.V., P.O. Box 1205, 8001 BE, Zwolle, the Netherlands
[d] European Synchrotron Radiation Facility, 71, Avenue des Martyrs, CS, 40220, 38043, Grenoble, Cedex 9, France
[e] Diamond Light Source Ltd., Didcot, Oxfordshire, OX11 0DE, UK
[f] KWR Water Research Institute, P.O. Box 1072, 3430 BB, Nieuwegein, the Netherlands
[g] Laboratory of Microbiology, Wageningen University & Research, Stippeneng 4, 6708 WE, Wageningen, the Netherlands

ARTICLE INFO

Editorial handling by: Wenfeng Tan

ABSTRACT

Aeration followed by rapid sand filtration is a common method in drinking water treatment to remove iron (Fe) and manganese (Mn) from anoxic groundwater. To ensure the successful removal of Fe and Mn within a single filter, several factors such as raw water characteristics, backwash procedures and chemical and microbial interactions with the filter medium need to be considered. Here, we assess the characteristics of a single medium rapid sand filter with highly efficient removal of Fe and Mn. Using synchrotron X-ray spectroscopy, we show that formation of ferrihydrite-type Fe oxides in the top of the filter (0–50 cm) accounts for >95 % of the removal of dissolved Fe^{2+} in the filter. Birnessite-type Mn- oxides, which are thought to be biogenic, form over a wider depth interval (0–110 cm). Results of 16S rRNA gene amplicon sequencing indicate a corresponding distinct vertical stratification of the microbial community, with potential iron-oxidizing *Gallionella*, *Leptothrix* and *Sideroxydans* dominating in the upper part of the filter, and nitrifiers being more prevalent deeper in the filter. Besides Fe and Mn-oxide, Fe-flocs and bacteriological hollow sheets form in the upper part of the filter. Both the Fe-flocs, hollow Fe-sheets and part of the Fe and Mn coatings are removed through backwashing, thereby reducing the pressure difference measured over the filter medium linked to clogging of pores (from 14 kPa to 1.5 kPa) and ensuring continued water flow. Backwashing removes part of the *Gallionella*, but this does not negatively impact the filter performance. Strikingly, SEM imaging with EDS mapping revealed alternating layers of Fe and Mn-oxides on the coated grains throughout the filter. This indicates slow mixing of the filter medium between the upper 30 cm and the rest of the filter during backwashing. Slow mixing likely contributes to continued success of the filter by ensuring homogeneous filter bed growth, while still allowing for stratification of the microbial community.

1. Introduction

Groundwater serves as a vital drinking water source globally. Redox-sensitive elements such as iron (Fe) and manganese (Mn) often are present in anoxic groundwater. To ensure the provision of safe water and prevent aesthetic problems and fouling of distribution infrastructure with metal (oxyhydr)oxides (henceforth termed metal-oxides), the removal of these elements is essential (Buamah et al., 2009; Vries et al., 2017). A commonly employed method for removing dissolved Fe^{2+} and Mn^{2+} from anoxic groundwater, without the use of chemical oxidants, involves aeration followed by rapid sand filtration. Despite the widespread use of this technology, the design and operation of sand filters

* Corresponding author.
E-mail address: s.haukelidsaeter@uu.nl (S. Haukelidsaeter).

https://doi.org/10.1016/j.apgeochem.2024.105904
Received 26 July 2023; Received in revised form 15 December 2023; Accepted 7 January 2024
Available online 10 January 2024

have predominantly relied on empirical knowledge from plant operators accumulating over the years. Consequently, a comprehensive understanding of the characteristics of a well-functioning filter and how removal efficiencies depend on water chemistry, regular backwashing and associated filter medium characteristics is lacking.

In sand filters with high oxygen concentrations (O_2 > 250 μM), dissolved Fe^{2+} precipitates with low crystallinity, such as ferrihydrite ($Fe_{8.2}O_{8.5}$ $(OH)_4$ $3H_2O$; Michel et al., 2010) form in the top of the filter through homogeneous, heterogeneous or biological oxidation (Van Beek et al., 2016). Homogeneous Fe^{2+} oxidation refers to the oxidation of Fe^{2+} by dissolved oxygen and subsequent hydrolysis and precipitation of Fe-flocs. The process is rapid at near-neutral pH and typically occurs already in the supernatant on top of the filter (Gude et al., 2018; Vries et al., 2017). Heterogeneous Fe^{2+} oxidation refers to a series of reactions with oxidation and precipitation following surface adsorption of Fe^{2+} (Tamura et al., 1980; Van Beek et al., 2016). The ferrihydrite formed in sand filters through both pathways is mostly present as globular nodules (diameter of 2–6 nm), characterized by a high degree of surface roughness and a large surface area (Carta et al., 2009; Sharma et al., 2002). Iron-oxidizing bacteria use Fe^{2+} as an electron donor and, thus, can contribute to Fe removal in rapid sand filters as well (de Vet et al., 2011; Gülay et al., 2013). Bacteria belonging to the genera *Gallionella* and *Leptothrix*, for instance, are known iron-oxidizers, and their activity leads to the presence of characteristic twisted stalks and hollow sheets, respectively, that can be detected microscopically (Chan et al., 2010; Krepski et al., 2012). However, some iron-oxidizing *Gallionella* and *Sideroxydans* species can also produce particulate Fe-oxides of an amorphous morphotype (Emerson et al., 2010; Lin et al., 2012).

In rapid sand filters, Mn^{2+} is usually removed through heterogeneous and/or biological oxidation. While heterogeneous oxidation leads to the formation of Mn(III) or Mn(III)/Mn(II)-oxides including hausmannite, manganite or feitknechtite (Inoué et al., 2019; Lan et al., 2017; Murray et al., 1985) microbially catalyzed Mn(II) oxidation results in the precipitation of Mn(IV)-phyllomanganates such as birnessite or todorokite (Kim et al., 2003; Tebo et al., 2004; Villalobos et al., 2003; Webb et al., 2005). Biological Mn^{2+} oxidation likely plays an important role in the start-up phase of sand filters, but when filters age, it is believed that Mn^{2+} oxidation becomes predominantly heterogeneous (Bruins et al., 2015). Birnessite has a high negative charge and is characterized by a typical coral or sponge-like structure that is visible using an electron microscope (Tan et al., 2010; Bruins et al., 2015). Microbially produced Mn-oxides cannot easily be distinguished from those formed through chemical oxidation based on imaging. Techniques such as micro-focused Mn K-edge X-ray spectroscopy, however, can be used to provide crucial information to distinguish biologically and chemically formed Mn-oxides by characterizing the redox state and local coordination environment of Mn (Zahoransky et al., 2022). Removal of Mn^{2+} in rapid sand filters can be hindered by high concentrations of Fe^{2+} or ammonium (NH_4^+) in the raw water, possibly due to lowering the contact time with the filter medium, or due to the reductive dissolution of Mn-oxides by Fe^{2+} (Gouzinis et al., 1998; Haukelidsaeter et al., 2023; Tian et al., 2019).

Regular backwashing of sand filters is necessary to remove metal-oxides and to restore hydraulic function (Ramsay et al., 2021). The upward flow of water and air leads to mixing of filter medium, with the largest displacement often occurring in the top of the filter (Ramsay et al., 2021). Nevertheless, this mixing may still lead to a homogeneous composition of the filter bed and microbial community composition, as suggested in a recent study (Corbera-Rubio et al., 2023), but whether this holds for rapid sand filters in general remains to be confirmed.

In this study, we assessed the chemical and microbiological processes contributing to successful Fe and Mn removal and the impact of backwash in a single medium rapid sand filter treating anoxic groundwater at a drinking water treatment plant (DWTP) in the Netherlands. We used a combination of advanced geochemical and microbiological analyses, including synchrotron X-ray spectroscopy, X-ray diffraction (XRD), sequential extractions, scanning electron microscopy (SEM) and 16S rRNA gene amplicon sequencing to identify the chemical and microbial processes taking place in the filter before and after backwash. We found evidence for a vertical stratification of microbiological processes contributing to Fe and Mn removal, while alternating Fe and Mn coatings were found on the filter medium throughout the filter, implying slow mixing and thereby homogenization of the chemical composition of the filter medium due to backwashing.

2. Materials and methods

2.1. Drinking water treatment plant

The DWTP investigated in this study is located in Laren, the Netherlands (52.24029°N, 5.20258°E) and is operated by Vitens N.V. The groundwater is extracted from 9 wells (8 vertical wells and 1 horizontal well) from an unconfined shallow aquifer (−13 m). The groundwater is anoxic and is mixed with slightly oxygenated shallow ground water in the wells, therefore raw water contains some oxygen (~60 μM). The treatment process consists of three steps, including aeration, single medium rapid sand filtration and granular activated carbon filtration (Supplementary Fig. 1).

The DWTP operates two rapid sand filters in parallel, each with an area of 40 m^2 and a filter medium thickness of ~2 m. The sand has an average diameter of 1.7–2.5 mm (porosity ~42%) and density of 2.6 g/cm^3. The supernatant level which is controlled with a valve in the outflow of the filter, is between 30 and 40 cm above the filter bed. The feed flow is ~220 m^3/h. One filter (Filter 1) was investigated in this study and has been in operation with this sand filter material since 2014, when the sand was replaced after ~25 years of operation. The DWTP is not continuously operational, with production periodically being halted when drinking water demands are lower. The annual production rate for Filter 1 is ~1 000 000 m^3.

Filters are backwashed after 16 000–18 000 m^3 water has been produced (every ~72–82 h). This cleaning procedure has a duration of 19.5 min and consists of the following steps: 1 min of water backwash (water velocity of 21 m/h), 12 min of air and water backwash (air velocity of 60 m/h, water velocity of 20 m/h and) and 6.5 min of water backwash (water velocity of 40 m/h). The backwash does not lead to overall bed expansion.

The pressure difference in the filter during a filter run is monitored continuously by the drinking water company using piezometers in the top and bottom of the filter. The pressure difference data for two backwash cycles which sampling was conducted in November 2021 were analyzed in this study. We also calculated the Fe load between two backwash cycles based on raw water concentrations and the total volume filtered, and assessed whether there was a relationship between the Fe load and pressure buildup.

2.2. Sample collection

Water samples were collected in November 2021 at five different times in a backwash cycle, first at the end of the runtime (74 h), then at four different time points after backwash (2 h, 25 h, 29 h and 43 h). Filter medium samples were obtained just before and after backwash (74 h, 0 h). Backwash suspension samples were collected every 1 min during the backwash procedure.

Extracted groundwater ("raw water") was collected prior to aeration. Filter influent water was collected directly from the supernatant water above the filter. To assess Fe^{2+}, Mn^{2+} and NH_4^+ removal in the filter, water samples were obtained from 6 taps available at the side of Filter 1 at 50, 80, 110, 140, 170 and 200 (bottom of filter) cm depth. Filter effluent water was sampled from a tap exiting under the filter effluent chamber.

The pH, O_2, conductivity and temperature were measured directly in the water from the taps with a HQ40D Portable Multimeter (HACH),

with a tube from each tap leading directly into a plastic bottle that overflowed continuously. Unfiltered and filtered (0.45 μm) water samples were collected in 15 mL centrifuge tubes and acidified with ultrapure nitric acid (HNO_3; 10 μL per 1 mL of sample) and stored at 4 °C for analysis of total and dissolved Fe and Mn. For the analysis of NH_4^+, NO_2^- and NO_3^-, separate filtered water samples were collected and stored at −20 °C.

A stainless-steel peat sampler (Veenlans 04.09, Royal Eijkelkamp) was used to collect sand samples at the following sand filter depth intervals for analysis of the geochemistry and microbiology: 0–2 cm, 4–6 cm, 10–15 cm, 15–20 cm, 25–30 cm, 30–40 cm, 40–50 cm, 50–60 cm, 60–70 cm, 70–80 cm, 80–90 cm, 90–100 cm, 100–110 cm, 110–120 cm, 120–130 cm, 130–140 cm, 140–150 cm, 150–160 cm and 160–170 cm. The sand samples were stored in 50 mL centrifuge tubes in a freezer (−20 °C) until analysis.

2.3. Analysis of water chemistry

Total and dissolved Fe (Limit of Detection [LOD] = 0.4 μM) and Mn (LOD = 0.018 μM) were analyzed using a PerkinElmer Avio 500 Inductively Coupled Plasma Optical Emission Spectrophotometer (ICP-OES). The difference between total and dissolved Fe and Mn was used as a measure of particulate Fe and Mn. The concentration of NH_4^+ (LOD = 0.3 μM), NO_2^- (LOD = 0.02 μM) and NO_3^- (LOD = 0.09 μM) in the filtered water samples was determined spectrophotometrically with a Gallery™ Discrete Analyzer. NO_x was measured as described in Jumppanen et al. (2014), and NH_4^+ according to ISO7150–1:1984.

2.4. Geochemical analysis of filter medium

The type of Fe and Mn-oxides present on the coatings before and after backwash was determined using a three-step sequential extraction procedure with ascorbic acid, 1 M HCl and CDB (Claff et al., 2010; Lenstra et al., 2021; Raiswell et al., 2010). The first extraction step with ascorbic acid primarily dissolves Fe from poorly crystalline Fe-oxides (e.g., ferrihydrite) and Mn-oxides (e.g., birnessite). The second extraction step dissolves minerals sensitive to low pH, including carbonates and poorly ordered oxides, and the third step dissolves crystalline Fe-oxides. The filter medium was freeze-dried prior to extraction. Approximately 100–250 mg of filter medium and 10 mL extractant were used in each step. All samples were analyzed with ICP-OES to determine Fe and Mn content.

For high-resolution imaging, coating thickness measurements and elemental mapping of coating characteristics, a Zeiss EVO 15 environmental SEM with energy dispersive X-ray spectroscopy (EDS) was used. Filter medium from 5 to 10 cm and 150–160 cm in the filter bed was analyzed, from samples taken before (74 h) and after backwash (0 h). Selected samples were freeze-dried and fixed to 0.5-inch aluminum SEM specimen stubs (Agar Scientific Ltd.) using a conductive carbon glue. Mounted samples were coated with 15 nm of platinum using a 208 H R Sputter Coater. Particles from backwash water (taken after 7 min of backwashing) were processed and analyzed in a similar manner.

Filter medium from 15 to 20 cm depth in the filter was embedded in epoxy resin (2.5 cm) and polished to expose cross sections of the sand grains and coatings at the surface. The sample was investigated using μ-XRF and μ-X-ray absorption spectroscopy at Fe and Mn K-edges at the ID21 beamline (Salomé et al., 2013) at the European Synchrotron Radiation Facility (ESRF) in Grenoble, France. The beam was focused to 0.7 μm ver. × 0.8 μm hor. Using a Kirkpatrick Baez mirrors system. The samples were mounted vertically, with an angle of 62° with respect to the incident beam. X-ray energy of the incoming beam was selected and tuned by means of a horizontal deflecting double-mirror system (Si coating for harmonics rejection) and a Si (111) monochromator (ΔE/E ~2.10−4). The beam intensity was monitored continuously using a photodiode placed upstream of the sample. XANES spectra were acquired in XRF mode, using a large area (80 mm^2 collimated active area) Silicon Drift Diode (Bruker, Karlsruhe, Germany). At selected spots, X-ray absorption spectra in fluorescence mode were collected within the corresponding energy range, 6.50–6.90 keV and 7.00–7.65 keV for Mn and Fe, respectively. The monochromator energy was calibrated based on the maximum intensity of the first derivative of Mn foil at 6.53862 keV for Mn and Fe foil at 7.11198 keV for Fe. X-ray fluorescence spectra were processed and I_0 normalized using the PyMca X-ray Fluorescence Toolkit (Sole'et al., 2007) to produce elemental maps. Spectra for analyzing the X-ray absorption near edge structure (XANES) and extended X-ray absorption fine structure (EXAFS) were normalized and extracted using the ATHENA software package (version 0.8.056 Ravel and Newville, 2005).

Consecutively collected Mn-XANES spectra at one spot exhibited a shift of the edge to lower energies and a decrease in white line intensity, indicating photoreduction of Mn-oxides (Supplementary Fig. 2). For this reason only the first spectrum was used for further analysis, assuming that the effect of photoreduction was negligible for this spectrum. Normalized Fe and Mn XANES spectra, collected at different spots on the sample, varied for the respective element regarding the amplitude of oscillations, shape and position of the edge, and the magnitude of the pre-edge feature. These differences could not be solely ascribed to differences in speciation but are also caused by self-absorption. To correct for self-absorption the XANES(Fluo) algorithm a correction method developed by Daniel Haskel implemented in Athena was used (Haskel, 1999). As the exact composition at the measured spots was not known the correction was made based on $Fe(OH)_3$ n (H_2O) and MnO_2 n (H_2O), respectively. The number of water molecules was adjusted until the magnitude of the pre-edge feature and the amplitude of the white line was similar to those of the selected reference spectra showing strong resemblance with the spectra from the sample. Differences among spectra remaining after this correction should then be indicative for differences in speciation. \

The mineralogy of Fe and Mn-oxide coatings from selected samples from the top (2–4 cm), middle (90–100 cm), and bottom (150–160 cm) of the filter was determined by XRD. Freeze dried samples were ground using a mortar and pestle and sieved to obtain the fraction <50 μm and subsequently placed onto a PMMA sample holder with a cavity diameter of 25 mm. XRD spectra were obtained with a Bruker D8 Advance with a LYNXEYE detector and a θ/θ goniometer with Cu-Kα radiation (λ = 1.54056 Å) with the tube operated at 40 kV and 40 mA. We used a primary Soller slit of 2.5°, a motorized divergence slit that illuminates 20 mm of the sample, resulting in a constant irradiated surface, and a motorized anti-scatter screen. X-ray powder diffraction patterns were recorded from 3 to 80 °2θ, in 0.02° steps, and counting for 0.85 s per step. Samples were spun continuously during measurement (0.25 Hz). Samples were compared to standards, including those of quartz and felspar minerals and, Fe and Mn-oxides (e.g. birnessite and ferrihydrite) for identification.

Specific surface areas of selected filter medium samples from 2 to 4 cm, 50–60 cm, 100–110 cm, and 150–160 cm were measured using the Brunauer-Emmett-Teller (BET) nitrogen gas adsorption method (relative pressure range 0.05–0.25) with a Quanta chrome Autosorb-6B gas adsorption analyzer at 77 K. Results were normalized to the density of the filter material. Before the surface area measurement, the samples were exposed to a vacuum for 40 h at 60 °C.

2.5. DNA isolation and 16S rRNA gene amplicon sequencing For analysis of the microbial community before and after backwash (74 h and 0 h), sand samples of the filter medium were analyzed from the following depth intervals for spatial coverage: 0–2 cm, 4–6 cm, 10–15 cm, 25–30 cm, 40–50 cm, 70–80 cm, 80–90 cm, 110–120 cm, 130–140 cm, 160–170 cm.

Genomic DNA was extracted from samples of 0.5 g (wet weight) using the DNeasy Powersoil DNA isolation kit (QIAGEN, Hilden, Germany). Cell lysis was performed by bead beating at 50 Hz for 1 min using a TissueLyser LT (QIAGEN, Hilden, Germany). When insufficient amounts of DNA were obtained, up to four replicates using 0.5 g sample

material each were pooled on one GeneJet Spin column. In addition to 800 μL CD1 solution, 500 μL of 10 % w/v skimmed milk (Sigma-Aldrich) was added to the Powerbead Pro tubes. The skimmed milk solution was autoclaved for 5 min at 121 °C, which proved long enough to avoid isolating DNA from the skimmed milk itself, and short enough to avoid excessive caramelizing of the skimmed milk solution (Corbera-Rubio et al., 2023). Prior to DNA elution in 100 μL DEPC water, the column was incubated with DEPC water for 1 min at room temperature.

16 rRNA gene amplicon sequencing was performed by Macrogen Inc. (Seoul, South Korea) using the Illumina MiSeq platform. Primers used for bacterial 16S rRNA gene amplification were 341 F (5′-CCTACGGGNGGCWGCAG-3′; Herlemann et al., 2011) and 806 R (5′-GGACTACHVGGGTWTCTAAT-3′; Caporaso et al., 2011). Paired end libraries were constructed using the Herculase II Fusion DNA Polymerase Nextera XT Index Kit V2 (Illumina, San Diego, USA) with the 16 S Metagenomic Sequencing Library Preparation Part # 15044223 Rev. B protocol. Between 100.000 and 260.000 paired end reads were obtained per sample. The data was processed in R (v3.5.1; R Core Team, 2019) using the DADA2 pipeline (v1.8; Callahan et al., 2016). The 16 S rRNA gene-based taxonomy was obtained using the SILVA database (release 138.1,Quast et al., 2012). The relative abundances as calculated using DADA2 were analyzed using the R package Phyloseq (v1.30.0; McMurdie and Holmes, 2013). For data visualization in bar plots, families and genera were included that constituted >1% and 1.5% relative abundance, respectively, in at least two of the samples.

3. Results

Before backwash (i.e. 74 h after the previous backwash cycle), the filter was covered with a 1–2 cm thick layer of fine orange flocs (Fig. 1 A). The color of the filter medium was reddish-brown in the top 30 cm of the filter and gradually transitioned to blackish-brown between ~50 and 160 cm depth (Fig. 1 B). Directly after backwash, the orange layer of fine material on top of the filter was no longer present and the color of the upper 30 cm of the filter was much browner (Fig. 1C). The deeper parts of the filter (below 50 cm depth) remained predominantly blackish-brown (Supplementary Fig. 3).

3.1. Water chemistry and filter functioning

The supernatant of the sand filter was always well-oxygenated (>280 μM O_2; Table 1) because of the aeration of abstracted anoxic groundwater prior to the sand filtration step. In the sand filter, oxygen concentrations decreased with depth, but never reached values below 193 μM (Fig. 2). Only minor variations in pH were observed, with values ranging from 7.2 to 7.4. The conductivity of the water decreased with depth in the filter (by ~10 units), in line with the removal of solutes. Both NH_4^+ and NO_3^- were present in the raw water (~34 and 50 μM, respectively). All NH_4^+ was converted to NO_3^- in the sand filter (Table 1; Supplementary Fig. 4).

Iron in the raw water was mostly present in dissolved form (Table 1). At the end of a filter run, particulate Fe dominated in the supernatant of the sand filter. After backwash, however, Fe in the supernatant of the sand filter was primarily dissolved (Fig. 2). The Fe data for 25 and 43 h h after backwash show that the proportion of particulate Fe increased at the expense of dissolved Fe during the filter run. Most Fe removal (>95–99 %) occurred in the top 50 cm of the filter at the investigated time points (Table 1 and Supplementary Data S2).

Manganese occurred only in dissolved form and is, therefore, assumed to be present as Mn^{2+}. Manganese was removed between a depth of 0 and 110 cm depth, in parallel with NH_4^+ (Fig. 2). At 50 cm depth in the filter, only ~52 % of the incoming Mn was removed. The depth of Mn removal and the removal efficiency did not change during the investigated time points of a filter run (Supplementary Data S1).

With increasing runtime, an increase in pressure across the filter from 1,5 kPa–14 kPa was observed (Fig. 3), which strongly correlated with the Fe load (R^2 = 0.93; Supplementary Data S3). After backwashing, the pressure across the filter was restored to1 kPa.

3.2. Filter medium

Most Fe-oxides were extracted in the ascorbic acid step, while Mn-oxides were mostly dissolved in HCl (Supplementary Table 1). The ratio of the total Mn:Fe extracted was close to 1, with an average of ~680 μmol/g Fe and ~674 μmol/g Mn-oxides present throughout the filter before and after backwash (Supplementary Table 1). If we combine the Fe and Mn load for the filter (see section 2.1, assuming a bulk filter material density of 2.6 g/cm^3 and 7 years of operation) with the total amount of Fe and Mn measured in the filter (average before and after backwash), we find that ~17% of the Fe and ~63% of the Mn that entered the filter accumulated there. This implies that ~83% of the Fe and ~37% of the Mn was removed from the filter through backwash (Supplementary Table 1, Supplementary Data S4).

The thickness of the mineral coatings ranged from ~80 to ~200 μm. Before backwash, Fe-oxides dominated the coating surface in the top 30 cm of the filter (Fig. 4, top 5 cm). After the filter was backwashed, a mix of both Fe and Mn-oxide surface-coated grains were found in the top of the filter. The Fe-oxides consisted of globular nodules <1 μm, while Mn-oxides appeared as sponge/coral like structures of 1–13 μm in diameter (Supplementary Figs. 5 and 6).

Cross-sections of the coatings revealed that they consisted of alternating layers of Fe and Mn-oxides (Fig. 4). The alternating coatings were

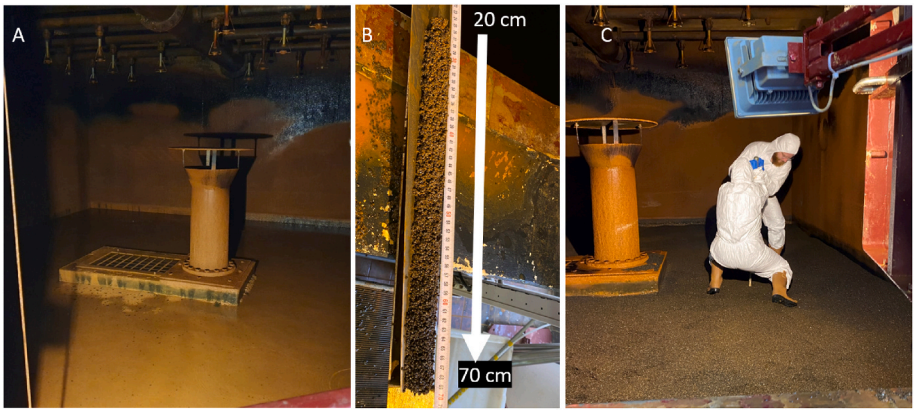

Fig. 1. Photos taken during sampling of the filter in November 2021. A) Drained filter surface before backwash (74 h). B) Filter medium as collected from a depth of 20–70 cm in the filter before backwash showing a color transition from reddish-brown to blackish-brown. C) Drained filter surface after backwash, also showing people collecting filter medium.

Table 1
Concentrations of Fe, Mn and NH_4^+ in rapid sand filters before (74 h) and after backwash (2h). Concentrations of total Fe, Mn, NH_4^+, O_2, pH, and conductivity in the raw water (Raw), supernatant (Sn), at 50 cm depth in the filter, and in the effluent (Eff). For data from the additional sampling time points, see Supplementary Data.

	Sample	Fe^{2+} dissolved	Fe particulate	Mn dissolved	NH_4^+	NO_3^-	O_2	pH	Conductivity
		µM	µM	µM	µM	µM	µM		µS/cm
74 h	Raw	52	1	17	35	55	70	7.3	474
	Sn	5	47	17	35	55	280	7.4	471
	50 cm	0.5	0.1	8	12	74	218	7.3	462
	Eff	0.2	0	0	0.3	96	193	7.3	460
2 h	Raw	53	0	17	34	54	69	7.2	474
	Sn	45	7	17	34	55	280	7.4	471
	50 cm	2	0.5	7	11	73	233	7.4	463
	Eff	0.4	0.1	0	0.4	86	243	7.3	460

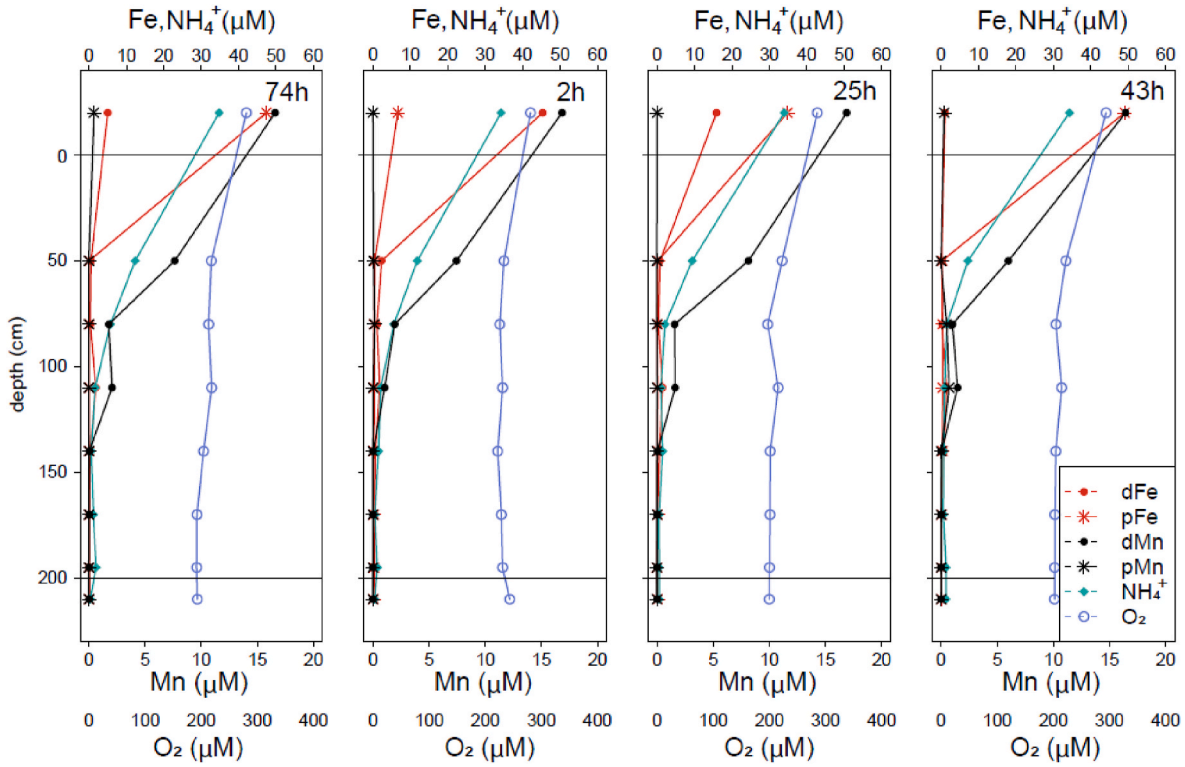

Fig. 2. Depth profiles of Fe, Mn, NH_4^+ and O_2 in the filter. A) 74 h runtime (just before backwash), B) 2 h, C) 25 h, and D) 44 h runtime after backwash. Dissolved Fe (dFe, red bullets), particulate Fe (pFe, red stars), dissolved Mn (dMn, black bullets), particulate Mn (pMn, black stars), NH_4^+ (light green diamonds) and O_2 (purple hollow bullets), concentrations at different depths in the filter are shown.

found on filter medium grains originating from both the surface (top 5 cm) and bottom samples (150 cm). Given the more than seven years of operation of the sand filter at the time of sampling, this suggests slow mixing of the filter medium over the full filter depth, and not only the top ~50 cm. The Mn-oxide layers were more porous compared to the denser Fe-oxide layers (Supplementary Fig. 7). The BET specific surface area of the filter medium was similar across all depths of the filter (~3.4 × 10^7 m^2/m^3; Supplementary Data S5).

Remnants of hollow sheets, characteristic for the iron-oxidizer *Leptothrix* (Emerson et al., 2010) and twisted stalks resembling those known for *Gallionella* (Chan et al., 2010) were detected on the metal coated surface of the filter medium, and, occasionally, were found to be intertwined within the filter medium coating (Fig. 5). The hollow sheets were far more dominant compared to the twisted stalks, with the highest abundance in the top 30 cm of the filter. EDS imaging confirmed that the hollow sheets mainly consist of Fe-oxides (Fig. 5B). Bacterial filaments on the filter medium coating, recognizable by their enrichment in carbon, were also detected (Fig. 5A).

Self-absorption corrected XANES and EXAFS spectra of Fe and Mn collected along a transect through the coating did not show significant differences (Fig. 6). This indicates that the redox state and speciation of Fe and Mn in the coating is very similar, irrespective of position and, hence, age and change in composition. Upon comparison with spectra from a variety of Fe-oxides the XANES spectra and the part of the EXAFS spectra with acceptable quality (k < 7 Å-1) showed closest resemblance with the spectrum FhSi*. This spectrum is a combination of spectra collected from Fe(III) precipitates formed upon the oxidation of Fe^{2+} in the presence of 0.5 mM silicic acid in Na and Ca containing background electrolyte (Senn et al., 2015). These precipitates are generally poorly ordered and characterized by a lower degree of corner-sharing polymerization compared to 2 L ferrihydrite, synthesized in the absence of Si. The position of edge of the Mn XANES spectra indicates that Mn is predominately in the form of Mn(IV) and the XANES and EXAFS spectra showed closest resemblance with those of hexagonal birnessite produced by Mn(II) oxidation by *Pseudomonas putida*. However, the quality of the EXAFS spectrum beyond k 8 Å-1 was insufficient to unequivocally identify the structure of the phyllomanganates as distinctive features in the EXAFS spectra are located in that region (Webb et al., 2005).

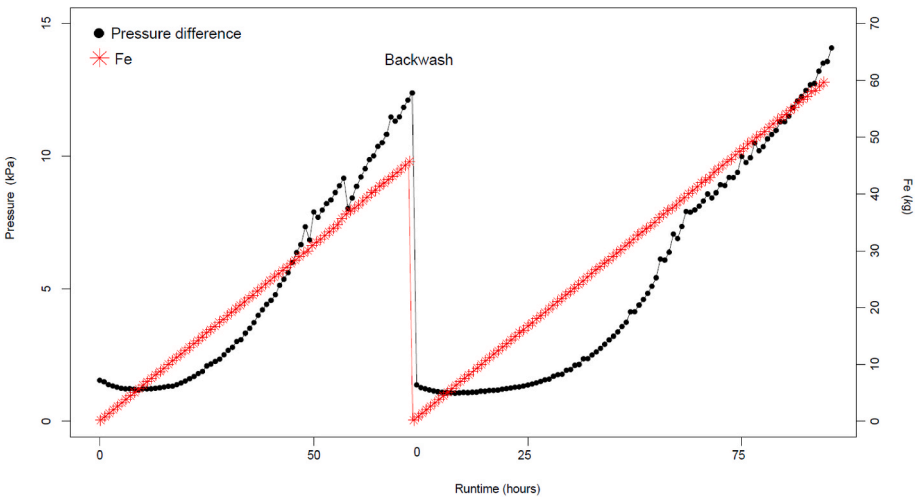

Fig. 3. Pressure difference buildup in the filter as a function of filtration runtime in two backwash cycles. Pressure (black dots) and Fe load (red stars) over filter runtime are shown. The Fe load is estimated based on raw water concentrations (kg).

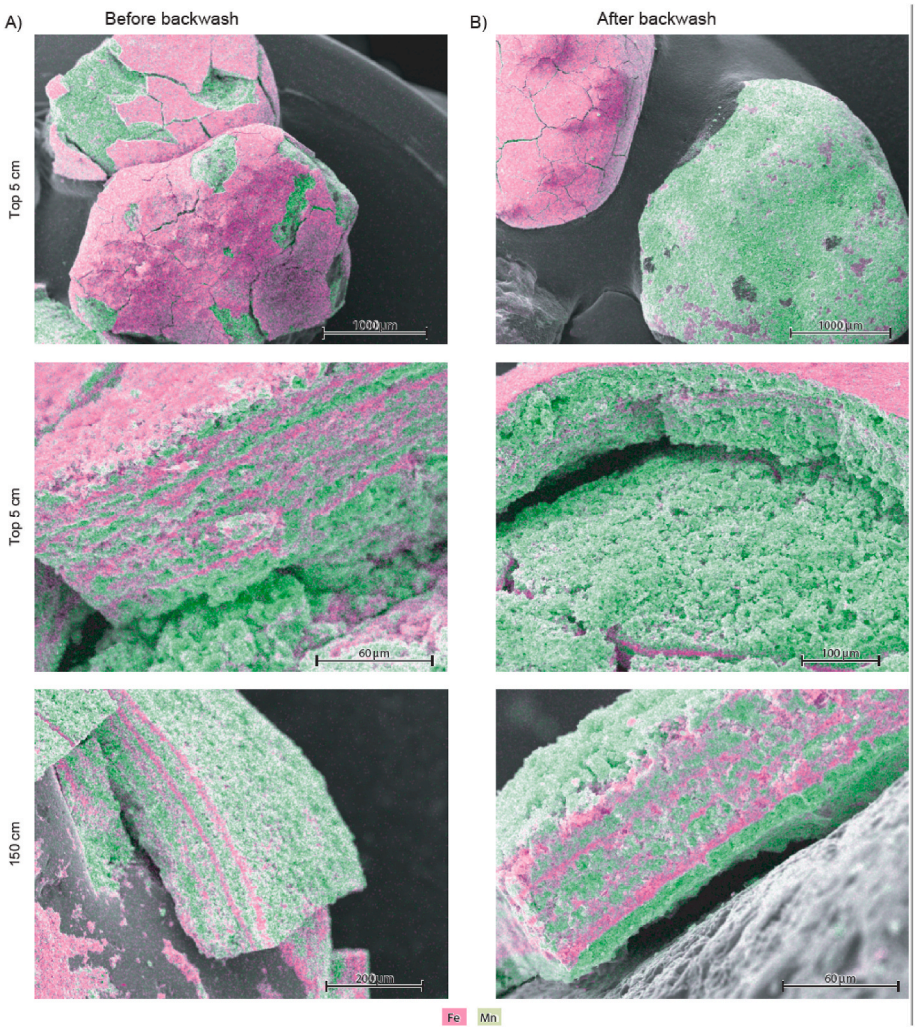

Fig. 4. SEM-EDS images of filter medium coatings. A) before backwash (74 h) and B) after backwash (0 h). Samples were taken from the top (5 cm) and bottom (150 cm) of the filter. Fe is shown in pink, Mn in green.

No sharp peaks other than those attributed to quartz and feldspar (microcline) could be identified in the X-ray diffractograms (Supplementary Fig. 8). This is in line with the findings from XAS analysis as ferrihydrite-like precipitates and biogenic birnessite only produce broad peaks with low amplitude (Cornell and Schwertmann, 2003; Villalobos et al., 2003).

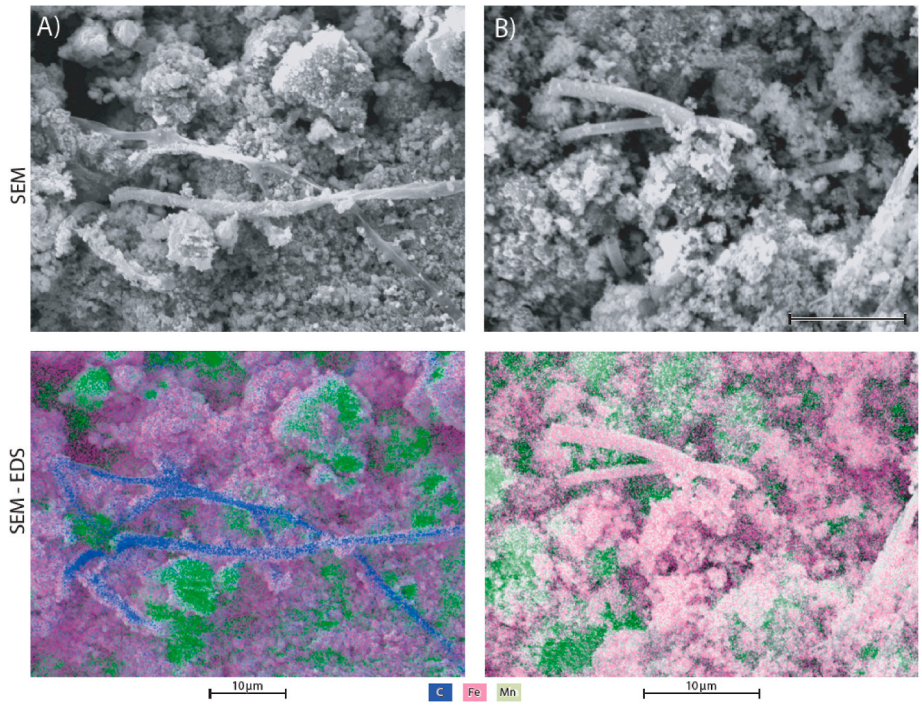

Fig. 5. High resolution SEM and SEM-EDS images of microbial features on the filter medium. Sample was taken at 5 cm depth after backwash. A) Uncoated carbon-containing bacterial filaments and Mn-rich globular sponge-like structures; B) Fe-rich hollow sheets and Mn-rich globular sponge-like structures. Fe is indicated in pink, Mn in green and carbon (C) in blue.

SEM analysis of the backwash suspension showed that the backwash process mainly removed Fe-flocs and we observe bacterial Fe-deposit structures mainly in the form of hollow sheets. Furthermore, some Mn-oxides were detected in these Fe-flocs, indicating that Mn was also removed during backwash (Supplementary Fig. 8).

3.3. Microbiology

The results of 16S rRNA gene amplicon sequencing revealed distinct variations in the microbial community with filter depth that largely remained undistributed by the backwashing procedure (Fig. 7). Before backwash, *Gallionella* was the most abundant genus in the upper 30 cm of the filter (40% and 20% at 2 cm and 30 cm, respectively), but decreased in relative abundance with depth to 0.4% at the bottom of the filter. Below 40 cm, *Candidatus* Nitrotoga constituted the most abundant genus in the *Gallionellaceae* family (Supplementary Fig. 10). Additionally, the genera *Leptothrix* and *Sideroxydans* were present at 3–6% and 3–7%, respectively, with the highest abundance in the top 30 cm.

The relative abundance of *Nitrospira* increased with depth in the filter, accounting for ~5% across the top 30 cm to ~18% at 160 cm depth. Generally, the microbial community below 100 cm depth was more diverse than in the top of the filter (Fig. 7).

Just after the filter was backwashed, the abundance of *Gallionella* in the top of the filter decreased (from 45% to 20% at cm depth), while the relative abundances of *Sideroxydans* and *Leptothrix* did not decrease. The relative abundance of *Nitrospira* increased in the first 30 cm of the filter, from ~5% to ~7% before and after backwash, respectively. Generally, the microbial community below 25–30 cm depth in the filter remained unchanged after backwash, as supported by nonmetric multidimensional scaling (NMDS) analysis, which showed samples from similar depths from before and after backwash clustering together (Supplementary Fig. 11).

4. Discussion

4.1. Mechanisms of Fe and Mn removal

In this study, we show that both Fe^{2+} and Mn^{2+} are successfully removed during drinking water production from abstracted groundwater, using one single-media rapid sand filtration step. This removal is the result of a combination of both chemical and microbiological processes and requires regular backwashing to counteract pressure buildup in the filter.

Because of fast oxidation of Fe^{2+} under oxygenated conditions (Gude et al., 2018), most Fe^{2+} is removed in the supernatant and settles as Fe-flocs and microbially formed Fe-oxides on the filter bed (Figs. 1 and 5). As the water flows through the filter bed, globular nodules of Fe-oxides are formed on the filter medium in the form of coatings, indicating that heterogeneous Fe^{2+} oxidation also plays a role in Fe^{2+} removal (Supplementary Fig. 5).

Gallionella, Leptothrix and *Sideroxydans* are genera known to harbor iron-oxidizing species that oxidize Fe^{2+} and dominate the top 30 cm of the filter (Fig. 7). This dominance, together with the observation of hollow sheets and twisted stalks indicative of biological iron-oxidation implies that microorganisms contribute to Fe^{2+} removal at this DWTP (Fig. 5). Even though some *Leptothrix* species can oxidize both Fe^{2+} and Mn^{2+} (Fleming et al., 2014; Zhang et al., 2002), our SEM-EDS mapping only reveals Fe-rich bacteriological hollow sheets, suggesting that *Leptothrix* mainly convert Fe^{2+} in the studied filter (Fig. 5). Some iron-oxidizing bacteria may enter the filter through the groundwater, as the raw water is mixed with oxygenated water in the wells already. Despite the general perception of Fe(II) oxidation being microaerophilic (e.g. Maisch et al., 2019), their presence and activity at higher O_2 concentrations, as observed here ($[O_2]$ = >70 µM; Table 1; Fig. 2), is common in drinking water treatment plants (de Vet et al., 2011; Gülay et al., 2018; Sharma et al., 2005; Van Beek et al., 2016). Raw water containing iron-oxidizing bacteria has previously also been observed at other treatment locations (Pacini et al., 2005). The temperature of ~11 °C in the DWTP may further stimulate microbial iron-oxidation as

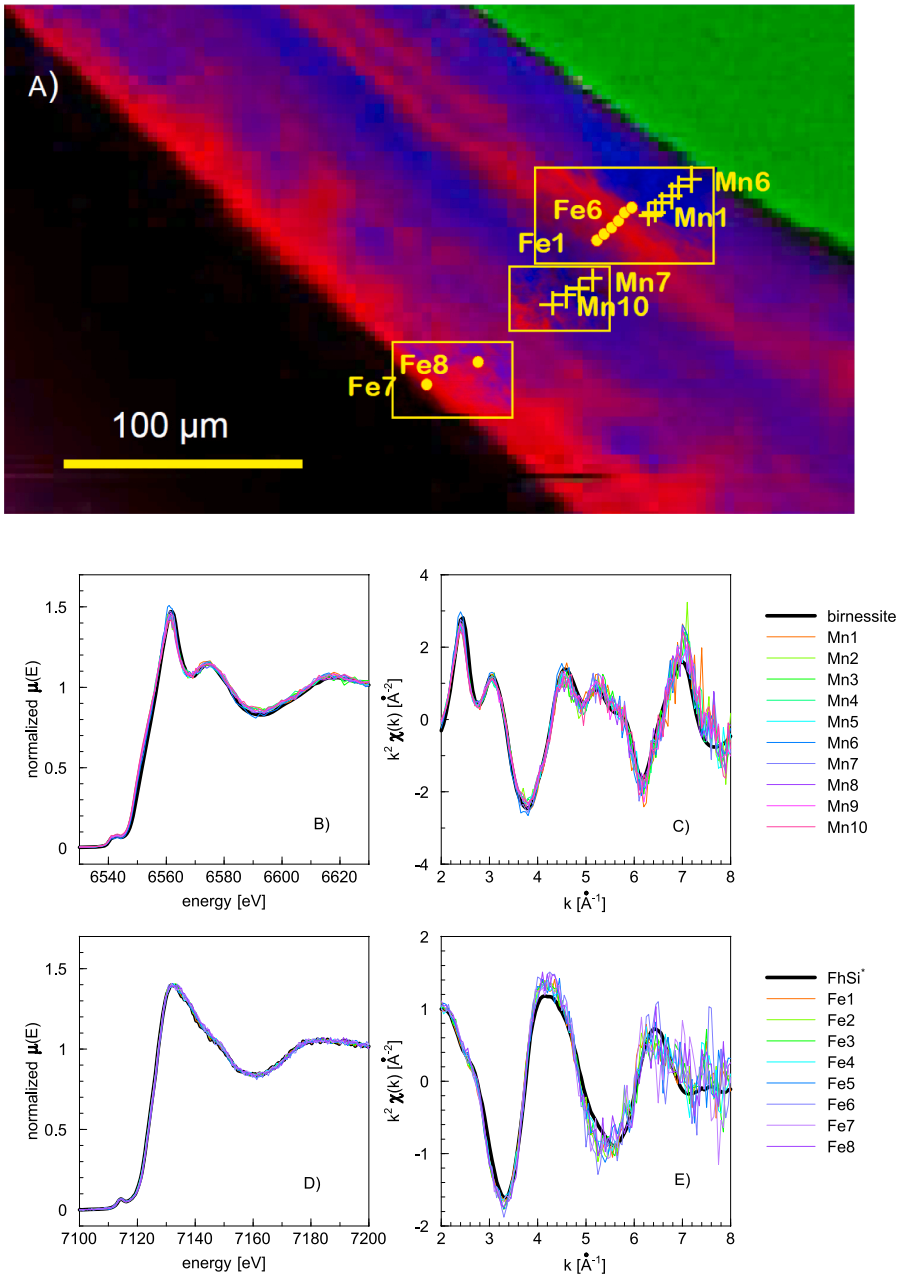

Fig. 6. XAS-spectra indicating mineralogy and oxidation state between the alternating Fe and Mn-oxide layers in the coating A) Elemental map showing alternating Fe (red) and Mn (Blue) layers on a sand grain containing Si (green) and the locations on the coating for which X-ray absorption spectra for Fe (yellow dots) and Mn (yellow crosses) were obtained. The large map has been collected with a step size of 2 µm while the rectangles indicate area of interests mapped with a resolution of 0.5 µm. Self-absorption corrected B) Mn XANES and C) Mn EXAFS spectra for 10 locations on the coating and for microbial, hexagonal birnessite, and D) Fe XANES and E) Fe EXAFS for 8 locations on the coating and the Fe–Si* spectrum obtained from Senn et al. (2015).

suggested in other studies (de Vet et al., 2011; Gülay et al., 2018). Notably, the bacterial production of Fe-oxides in the form of stalks and sheets may allow for longer runtimes, as bacterially produced Fe-oxides is slightly less voluminous compared to Fe-flocs formed through chemical precipitation (Sharma et al., 2005).

Both the solute and solid phase analyses indicate that removal of Mn^{2+} occurs down to a depth of 110 cm, in parallel with NH_4^+ removal (Fig. 2). The groundwater at this DWTP contains ~20 µM Mn^{2+}, which is a relatively high concentration compared to those elsewhere (Tekerlekopoulou et al., 2013). We note that the presence of NH_4^+ (~30 µM) does not negatively affect Mn^{2+} removal. This is in agreement with other studies showing that when NH_4^+ concentrations are below ~40 µM, Mn^{2+} and NH_4^+ can be removed in parallel (Tian et al., 2019). However, at higher NH_4^+ concentrations, Fe^{2+} and NH_4^+ removal typically occurs before Mn^{2+} removal (Corbera-Rubio et al., 2023). While the effect of high NH_4^+ concentrations on Mn^{2+} removal was previously linked to variations in O_2 and pH associated with nitrification (Gouzinis et al., 1998; Tian et al., 2019), other chemical, physical and/or microbiological factors likely also play a role in achieving successful Mn^{2+} removal in the presence of NH_4^+ (Haukelidsaeter et al., 2023).

Microbial Mn^{2+} oxidation is crucial in facilitating the removal of Mn^{2+} in the studied filter, as indicated by the dominance of Mn(IV) containing phyllomanganates in the oxide coatings (Fig. 6). Although we cannot exclude that heterogeneous oxidation of Mn occurs in the filter, the characteristic of Mn(III) and Mn(II)/Mn(III)-oxides with distinctively different XANES and EXAFS spectra were not found (Fig. 6;

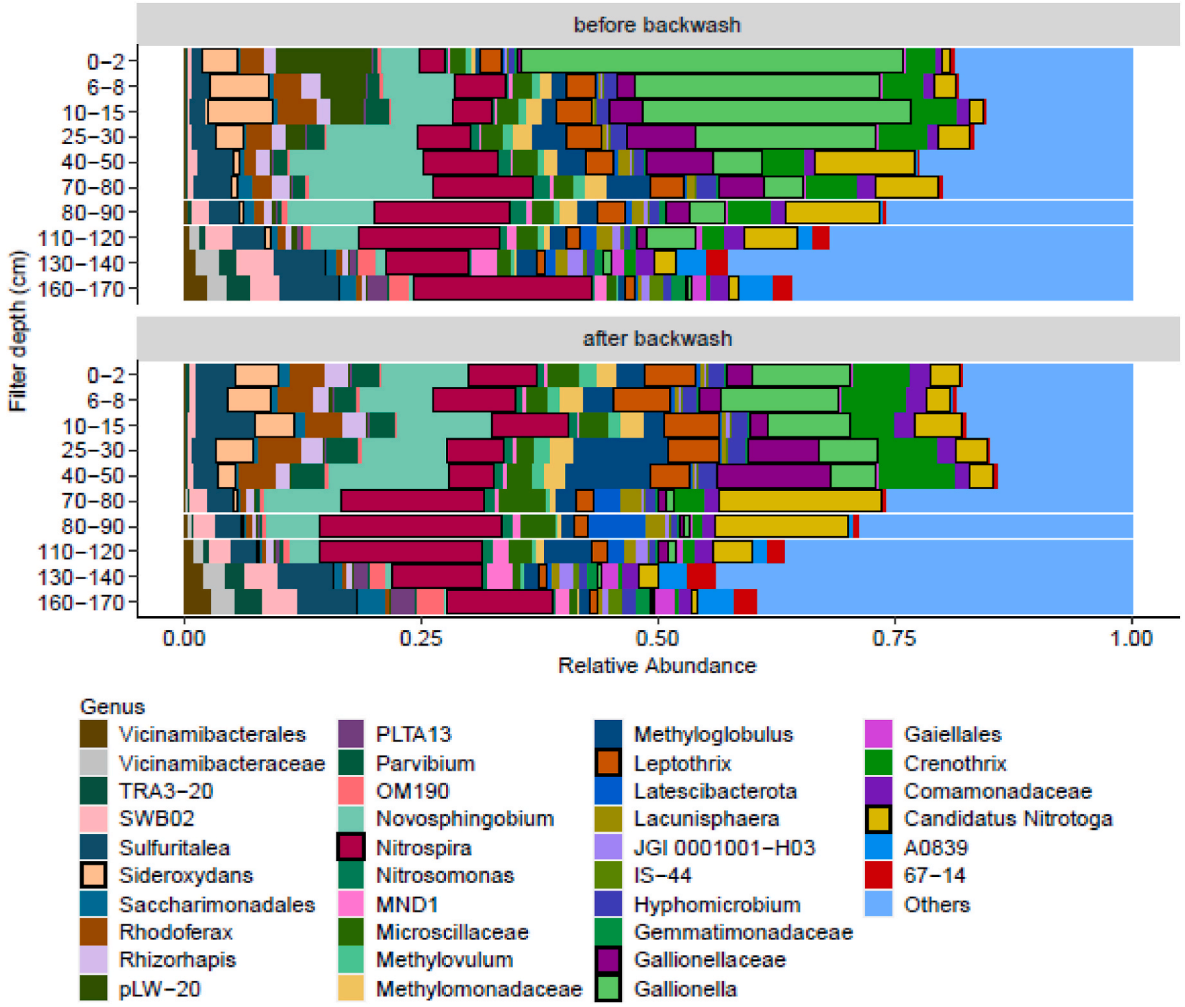

Fig. 7. Microbial community genus composition before and after backwash. 16S rRNA gene amplicon sequencing-based relative microbial abundances A) before backwash B) and after backwash. *Sideroxydans*, *Nitrospira*, *Gallionella*, *Leptothrix* and *Candidatus* Nitrotoga are highlighted.

Inoué et al., 2019; Murray et al., 1985). This contrasts with previous work on other DWTPs, which suggested heterogeneous oxidation of Mn^{2+} dominates after a mineral coating is established on the filter medium (Bruins et al., 2015). Members of the genus *Hyphomicrobium* are commonly encountered at drinking water facilities where Mn^{2+} is removed (Albers et al., 2015; Haukelidsaeter et al., 2023). While they may be involved in Mn^{2+} oxidation at this site, their abundance was low in the filter (Fig. 7). Additionally, the possibility for Mn^{2+} oxidation by nitrifying bacteria has been raised (Vandenabeele et al., 1995), which could match the simultaneous removal of Mn^{2+} and NH_4^+ as observed here (Fig. 2) and the large relative abundance of especially the genus *Nitrospira* (Fig. 7). However, based on 16S rRNA gene amplicon sequencing alone, we cannot deduce the microorganisms responsible for Mn^{2+} oxidation in this rapid sand filter.

The microbial depth stratification observed in the filter cannot be explained purely by thermodynamics, but rather indicates that there are unknown microbial and chemical interactions determining the sequence of microbial Fe^{2+}, Mn^{2+} and NH_4^+ oxidation in the rapid sand filters (Fig. 2; Fig. 7). In the top of the filter, iron-oxidizing bacteria need to rapidly oxidize Fe^{2+} in order to compete with chemical oxidation of Fe^{2+} (Emerson et al., 2010). Notably, Fe^{2+} oxidation precedes NH_4^+ oxidation in the filter, even though the latter process is thermodynamically more favorable (−58 kJ/mol for Fe^{2+} vs −349 kJ/mol for complete NH_4^+ oxidation; Emerson et al., 2010; Van Kessel et al., 2015). The inhibition of NH_4^+ removal by Fe has previously been observed in other drinking water filters (de Vet et al., 2009). The exact nature of this interaction has not yet been identified, however.

Subsequent removal of NH_4^+, occurring either prior to or at the same time as Mn^{2+} removal has also been observed at other DWTPs (Corbera-Rubio et al., 2023; Gouzinis et al., 1998; Tian et al., 2019). Again thermodynamics cannot fully explain this (−68 kJ/mol for oxidation of Mn^{2+} vs −349 kJ/mol for complete NH_4^+ oxidation; Yu and Leadbetter, 2020; Van Kessel et al., 2015), hence we assume that also here other, yet unidentified factors regulate this sequence. As the common terminal electron acceptor in all these reactions is O_2, and O_2 never becomes limiting in the investigated filter, its availability cannot be a cause of the zonation of microbial processes.

Importantly, the vertical structure of the microbial community within the rapid sand filter in this study exhibits a greater variation over depth compared to that of two other DWTPs (Fig. 6; Corbera-Rubio et al., 2023). This difference may be attributed to variations in backwash regimes implemented at these other locations and/or lower spatial sampling resolution with depth. Overall, the microbial depth distribution achieved here shows that regularly backwashed rapid sand filters can be biologically more heterogeneous than previously assumed.

4.2. *Effect of backwash*

The removal efficiency of the sand filter for Fe^{2+} and Mn^{2+} did not change during a filter run (Fig. 2). Hence, the backwash primarily restored efficient flow in the filter (Fig. 3). Without backwash, the pressure buildup in the filter would probably result in irregular and

preferential flow through the bed and uncontrollable supernatant level, which would negatively affect both Fe and Mn removal.

Despite higher concentrations of Fe in the raw water when compared to Mn (Table 1; Fig. 2), we show that the metal oxide coatings were equally enriched in Fe and Mn (Supplementary Table 1). The more efficient removal of Fe is the result of a difference in the removal mechanisms of Fe and Mn: while both Fe and Mn form coatings on the filter medium, Fe additionally forms flocs in the supernatant. Both the flocs and Fe and Mn-coatings are removed during backwash, together with mainly hollow sheets formed by iron-oxidizing bacteria (Supplementary Fig. 9).

We show that one backwashing event leads to substantial mixing of the upper 30 cm of the filter medium, while keeping both the stratification of the microbial community (Fig. 7) and the color gradient below a depth of 30 cm in the filter largely intact (Fig. 1). The most prominent change in the microbial community was the decrease in relative abundance of *Gallionella* in the top of the filter after backwash, indicating preferential loss of these iron-oxidizing bacteria.

The presence of layered Fe and Mn-oxide coatings, along with relatively uniform coatings throughout the height of the filter bed, indicates that slow mixing processes occur over time scales far beyond a single backwash cycle (Fig. 4, Supplementary Table 1). This is consistent with other studies indicating random grain displacement, eventually resulting in a more even distribution of the grains (Ramsay et al., 2021), and a homogenous chemical composition of the filter (Corbera-Rubio et al., 2023; Sharma et al., 2002). However, the clear stratification of the microbial community, indicates that full mixing is slower than bacterial regrowth within the different depths of the filter (Fig. 7).

The resulting uniform growth of the filter bed, stimulated by multiple backwash cycles is likely important for the hydrological performance of the filter (Ramsay et al., 2021). A well-sorted medium ensures a more homogeneous flow through the filter and increases the contact time between water and sand grains, which is especially crucial for effective Mn^{2+} removal (Haukelidsaeter et al., 2023).

4.3. Coating growth and ageing of rapid sand filters

Based on the measured coating thicknesses, a coating growth rate of 9–28 μm/year of the filter medium can be estimated (Fig. 6). A thick coating has been proven to be beneficial for microorganisms, such as nitrifiers, that colonize the outer periphery of the coating which acts as a protective layer during backwash (Gülay et al., 2014). We find that Mn-oxides are more porous than Fe-oxides, hence Mn-oxide coatings might provide more attachment surfaces for microorganisms. Because ~50% of the coating in the filter studied here consists of Mn-oxides, it is expected that at DWTPs where Mn^{2+} concentrations are lower and where the filter is operated under similar conditions, coatings on filter medium would have a lower rate of formation.

Combined X-ray characterization show that the Fe-oxide coating mainly consisted of ferrihydrite-like precipitates, which is in line with other research (Sharma et al., 2002). Ferrihydrite is thermodynamically more unstable compared to more crystalline oxyhydroxides, however the combined effect of the presence of Si and Ca during Fe^{2+} oxidation and precipitation can effectively retard aging of the precipitates and the formation of more stable phases (Senn et al., 2015), and likely also contribute to the preservation of the initially formed precipitates in the sand filter.

With time, the thickness of the filter medium coating increases. Once the grain sizes exceed a diameter of 3 mm (nearly 50% growth) the expansion of the bed during backwash can become inefficient, necessitating filter replacement.

5. Conclusions and implications for drinking water production

We find that chemical and biological removal mechanisms contribute to Fe and Mn at the drinking water treatment plant (DWTP) studied here. We show that biological removal processes play a role in Fe^{2+} removal, with iron-oxidizers such as Gallionella, Leptothrix, and Sideroxydans contributing to Fe removal, mainly in the upper 30 cm the filter. The uniformity of the birnessite (IV) minerals suggest microbial Mn^{2+} oxidation.

Our research highlights that the effectiveness of Fe and Mn removal from anoxic groundwater in drinking water production using single-media rapid sand filters strongly depends on the following factors:

1. **Raw water characteristics**: The initial concentrations of Fe and Mn can significantly impact the filtration efficiency and rate of coating formation, as Mn contributes more to coating formation compared to Fe. We observe that, at least at low NH_4^+ concentrations, Mn and NH_4^+ were removed in parallel.
2. **Regular backwashing:** Implementing an appropriate backwash procedure is vital for successful Fe and Mn removal. We show that pressure increases in the filters over a runtime, mainly due to the build-up of Fe-flocs that settle at the top of the filter. Backwash removes the Fe-flocs and Mn-oxides, thereby sustaining water flow. In the investigated filter, a single backwash cycle mainly mixed the upper ~30 cm of the filter. However, with time, backwashing does slowly mix the whole filter bed ensuring homogeneous growth of the coatings in the filter bed.
3. **Coating growth and coating formation:** The formation of mineral coatings improve both Fe^{2+} and Mn^{2+} removal, by providing sites for heterogeneous oxidation and attachment sites for microbes. The estimated rate of growth of the coating at the studied DWTP was ~9–28 μm per year.

Based on the above, we recommend that water treatment facilities control the backwash process to remove flocs without complete mixing of the filter media. This will likely be beneficial for the microbial processes taking place in the filter and ensure the reliable and effective removal of Fe and Mn, and ultimately provide high-quality drinking water to consumers.

CRediT authorship contribution statement

Signe Haukelidsaeter: Investigation, Methodology, Writing – original draft, Writing – review & editing. **Alje S. Boersma:** Formal analysis, Investigation, Methodology. **Lina Piso:** Investigation, Methodology. **Wytze K. Lenstra:** Investigation. **Niels A.G.M. van Helmond:** Resources. **Frank Schoonenberg:** Investigation, Resources, Validation. **Erik van der Pol:** Investigation, Resources. **Luis C.C. Hurtarte:** Formal analysis, Investigation. **Paul W.J.J. van der Wielen:** Supervision. **Thilo Behrends:** Methodology, Supervision. **Maartje A.H.J. van Kessel:** Supervision. **Sebastian Lücker:** Supervision. **Caroline P. Slomp:** Supervision.

Declaration of competing interest

The authors declare that they have no known competing financial interests or personal relationships that could have appeared to influence the work reported in this paper.

Data availability

I have shared the data in the attachement

Acknowledgements

We are grateful to Vitens N.V. for their support and collaboration during the visits to the drinking water plant. We also thank J. Visser, E. Hellebrand, J.J. Mulder and A. van Leeuwen-Tolboom for analytical support. This research was funded by the Netherlands Organisation for Scientific Research (NWO) partnership program Dunea–Vitens: Sand

Filtration (grant 17841). MAHJvK and SL were funded by NWO (016. Veni.192.062 and 016. Vidi.189.050, respectively), CPS by the European Research Council (ERC Synergy Grant 694407 MARIX).

Appendix A. Supplementary data

Supplementary data to this article can be found online at https://doi.org/10.1016/j.apgeochem.2024.105904.

References

Albers, C.N., Ellegaard-Jensen, L., Harder, C.B., Rosendahl, S., Knudsen, B.E., Ekelund, F., Aamand, J., 2015. Groundwater chemistry determines the prokaryotic community structure of waterworks sand filters. Environ. Sci. Technol. 49 (2), 839–846. https://doi.org/10.1021/es5046452.

Bruins, J.H., Petrusevski, B., Slokar, Y.M., Huysman, K., Joris, K., Kruithof, J.C., Kennedy, M.D., 2015. Biological and physico-chemical formation of Birnessite during the ripening of manganese removal filters. Water Res. 69 (0), 154–161. https://doi.org/10.1016/j.watres.2014.11.019.

Buamah, R., Petrusevski, B., de Ridder, D., van de Wetering, T.S.C.M., Shippers, J.C., 2009. Manganese removal in groundwater treatment: practice, problems and probable solutions. Water Sci. Technol. Water Supply 9 (1), 89–98. https://doi.org/10.2166/ws.2009.009.

Callahan, B.J., Mcmurdie, P.J., Rosen, M.J., Han, A.W., Johnson, A.J.A., Holmes, S.P.. dada2: high-resolution sample inference from illumina amplicon data, 13(7). https://doi.org/10.1038/nMeth.3869.

Caporaso, JG, Lauber, CL, Walters, WA, Berg-Lyons, D, Lozupone, CA, Turnbaugh, PJ, Fierer, N, Knight, R, 2011. Global patterns of 16S rRNA diversity at a depth of millions of sequences per sample. Proc Natl. Acad. Sci. USA. 108 (Suppl), 4516–4522. https://doi.org/10.1073/pnas.1000080107.

Carta, D., Casula, M.F., Corrias, A., Falqui, A., Navarra, G., Pinna, G., 2009. Structural and magnetic characterization of synthetic ferrihydrite nanoparticles. Mater. Chem. Phys. 113 (1), 349–355. https://doi.org/10.1016/j.matchemphys.2008.07.122.

Chan, C.S., Fakra, S.C., Emerson, D., Fleming, E.J., Edwards, K.J., 2010. Lithotrophic iron-oxidizing bacteria produce organic stalks to control mineral growth: implications for biosignature formation. ISME J. 5 (4), 717–727. https://doi.org/10.1038/ismej.2010.173.

Claff, S.R., Sullivan, L.A., Burton, E.D., Bush, R.T., 2010. A sequential extraction procedure for acid sulfate soils: partitioning of iron. Geoderma 155 (3–4), 224–230. https://doi.org/10.1016/J.GEODERMA.2009.12.002.

Corbera-Rubio, F., Laureni, M., Koudijs, N., Müller, S., Alen, T. Van, Schoonenberg, F., Lücker, S., Pabst, M., Loosdrecht, M.C., Van, M., Halem, D. Van, 2023. Meta-omics profiling of full-scale groundwater rapid sand filters explains stratification of iron, ammonium and manganese removals. Water Res. 233 (2023), 119805 https://doi.org/10.1016/j.watres.2023.119805.

Cornell, R.M., Schwertmann, U., 2003. The iron oxides: structure, properties, reactions, occurrence and uses. Corrosion Sci. 664 https://doi.org/10.1016/s0010-938x(97)00096-6.

de Vet, W.W.J.M., Dinkla, I.J.T., Rietveld, L.C., van Loosdrecht, M.C.M., 2011. Biological iron oxidation by Gallionella spp. in drinking water production under fully aerated conditions. Water Res. 45 (17), 5389–5398. https://doi.org/10.1016/j.watres.2011.07.028.

de Vet, W.W.J.M., Rietveld, L.C., Van Loosdrecht, M.C.M., 2009. Influence of iron on nitrification in full-scale drinking water trickling filters. J. Water Supply Res. Technol. - Aqua 58 (4), 247–256. https://doi.org/10.2166/aqua.2009.115.

Emerson, D., Fleming, E.J., Mcbeth, J.M., 2010. Iron-oxidizing bacteria: an environmental and genomic perspective. Annu. Rev. Microbiol. 64 (May), 561–583. https://doi.org/10.1146/annurev.micro.112408.134208.

Fleming, E.J., Cetinić, I., Chan, C.S., Whitney King, D., Emerson, D., 2014. Ecological succession among iron-oxidizing bacteria. ISME J. 8 (4), 804–815. https://doi.org/10.1038/ismej.2013.197.

Gouzinis, A., Kosmidis, N., Vayenas, D.V., Lyberatos, G., 1998. Removal of Mn and simultaneous removal of NH3, Fe and Mn from potable water using a trickling filter. Water Res. 32 (8), 2442–2450. https://doi.org/10.1016/S0043-1354(97)00471-5.

Gude, J.C.J., Joris, K., Huysman, K., Rietveld, L.C., van Halem, D., 2018. Effect of supernatant water level on as removal in biological rapid sand filters. Water Res. X 1, 1–10. https://doi.org/10.1016/j.wroa.2018.100013.

Gülay, A., Çekiç, Y., Musovic, S., Albrechtsen, H.-J., Smets, B.F., 2018. Diversity of iron oxidizers in groundwater-fed rapid sand filters: evidence of Fe(II)-Dependent growth by curvibacter and undibacterium spp. Front. Microbiol. 9 (December), 1–14. https://doi.org/10.3389/fmicb.2018.02808.

Gülay, A., Musovic, S., Albrechtsen, H.-J., Smets, B.F., 2013. Neutrophilic iron-oxidizing bacteria: occurrence and relevance in biological drinking water treatment. Water Sci. Technol. Water Supply 13 (5), 1295–1301. https://doi.org/10.2166/ws.2013.113.

Gülay, A., Tatari, K., Musovic, S., Mateiu, R.V., Albrechtsen, H.J., Smets, B.F., 2014. Internal porosity of mineral coating supports microbial activity in rapid sand filters for groundwater treatment. Appl. Environ. Microbiol. 80 (22), 7010–7020. https://doi.org/10.1128/AEM.01959-14.

Haskel, D., 1999. FLUO: correcting XANES for self-adsorption in fluoresence measurements, 1, 1–14.

Haukelidsaeter, S., Boersma, A.S., Kirwan, L., Corbetta, A., Gorres, I.D., Lenstra, W.K., Schoonenberg, F.K., Borger, K., Vos, L., Wielen, P.W., Van Der, J.J., Kessel, M.A., Van, H.J., Lücker, S., Slomp, C.P., 2023. Influence of filter age on Fe , Mn and NH + 4 removal in dual media rapid sand filters used for drinking water production. Water Res. 242 (June), 120184 https://doi.org/10.1016/j.watres.2023.120184.

Herlemann, D.P., Labrenz, M., Jü Rgens, K., Bertilsson, S., Waniek, J.J., Andersson, A.F., 2011. Transitions in bacterial communities along the 2000 km salinity gradient of the Baltic Sea. ISME J. 5, 1571–1579. https://doi.org/10.1038/ismej.2011.41.

Inoué, S., Yasuhara, A., Ai, H., Hochella, M.F., Murayama, M., 2019. Mn(II) oxidation catalyzed by nanohematite surfaces and manganite/hausmannite core-shell nanowire formation by self-catalytic reaction. Geochem. Cosmochim. Acta 258, 79–96. https://doi.org/10.1016/j.gca.2019.05.011.

Jumppanen, T., Jokinen, M., Airo, J., Klemm, M., Hoger, D., Suoniemi-Kähäräl, A., 2014. Automated Total Oxidized Nitrogen Method Using Vanadium as Reductant with Correlation to Cadmium and Hydrazine Reductant Methods in Sea, Natural, and Waste Waters. Thermo Fisher Scientific.

Kim, H.S., Pastén, P.A., Gaillard, J.F., Stair, P.C., 2003. Nanocrystalline todorokite-like manganese oxide produced by bacterial catalysis. J. Am. Chem. Soc. 125 (47), 14284–14285. https://doi.org/10.1021/ja0375784.

Krepski, S.T., Hanson, T.E., Chan, C.S., 2012. Isolation and characterization of a novel biomineral stalk-forming iron-oxidizing bacterium from a circumneutral groundwater seep. Environ. Microbiol. 14 (7), 1671–1680. https://doi.org/10.1111/j.1462-2920.2011.02652.x.

Lan, S., Wang, X., Xiang, Q., Yin, H., Tan, W., Qiu, G., Liu, F., Zhang, J., Feng, X., 2017. Mechanisms of Mn(II) catalytic oxidation on ferrihydrite surfaces and the formation of manganese (oxyhydr)oxides. Geochem. Cosmochim. Acta 211, 79–96. https://doi.org/10.1016/j.gca.2017.04.044.

Lenstra, W.K., Klomp, R., Molema, F., Behrends, T., Slomp, C.P., 2021. A sequential extraction procedure for particulate manganese and its application to coastal marine sediments. Chem. Geol. 584 (September), 120538 https://doi.org/10.1016/j.chemgeo.2021.120538.

Lin, C., Larsen, E.I., Nothdurft, L.D., Smith, J.J., 2012. Neutrophilic, microaerophilic Fe (II)-Oxidizing bacteria are ubiquitous in aquatic habitats of a subtropical Australian coastal catchment (ubiquitous FeOB in catchment aquatic habitats). Geomicrobiol. J. 29 (1), 76–87. https://doi.org/10.1080/01490451.2010.523446.

Maisch, M., Lueder, U., Laufer, K., Scholze, C., Kappler, A., Schmidt, C., 2019. Contribution of microaerophilic iron(II)-Oxidizers to iron(III) mineral formation [Research-article]. Environ. Sci. Technol. 53 (14), 8197–8204. https://doi.org/10.1021/acs.est.9b01531.

McMurdie, P.J., Holmes, S., 2013. Phyloseq: An R Package for Reproducible Interactive Analysis and Graphics of Microbiome Census Data. PLoS ONE 8 (4). https://doi.org/10.1371/journal.pone.0061217.

Michel, F.M., Barrón, V., Torrent, J., Morales, M.P., Serna, C.J., Boily, J.F., Liu, Q., Ambrosini, A., Cismasu, A.C., Brown, G.E., 2010. Ordered ferrimagnetic form of ferrihydrite reveals links among structure, composition, and magnetism. Proc. Natl. Acad. Sci. U.S.A. 107 (7), 2787–2792. https://doi.org/10.1073/pnas.0910170107.

Murray, J.W., Dillard, J.G., Giovanoli, R., Moers, H., Stumm, W., 1985. Oxidation of Mn (II): initial mineralogy, oxidation state and ageing. Geochem. Cosmochim. Acta 49 (2), 463–470. https://doi.org/10.1016/0016-7037(85)90038-9.

Pacini, V.A., Ingallinella, A.M., Sanguinetti, G., 2005. Removal of iron and manganese using biological roughing up flow filtration technology. Water Res. 39 (18), 4463–4475. https://doi.org/10.1016/j.watres.2005.08.027.

Quast, C., Pruesse, E., Yilmaz, P., Gerken, J., Schweer, T., Yarza, P., Peplies, J., Glöckner, F.O., 2013. The SILVA ribosomal RNA gene database project: improved data processing and web-based tools. Nucl. Acids Res 41 (D1), D590–D596.

Raiswell, R., Vu, H.P., Brinza, L., Benning, L.G., 2010. The determination of labile Fe in ferrihydrite by ascorbic acid extraction: Methodology, dissolution kinetics and loss of solubility with age and de-watering. Chem. Geol. 278 (1–2), 70–79. https://doi.org/10.1016/j.chemgeo.2010.09.002.

Ramsay, L., Du, F., Lund, M., He, H., Søborg, D.A., 2021. Grain displacement during backwash of drinking water filters. Water Sci. Technol. Water Supply 21 (1), 356–367. https://doi.org/10.2166/ws.2020.300.

Ravel, B., Newville, M., 2005 Jul. ATHENA, ARTEMIS, HEPHAESTUS: data analysis for X-ray absorption spectroscopy using IFEFFIT. J Synchrotron Radiat 12 (Pt 4), 537–541. https://doi.org/10.1107/S0909049505012719. Epub 2005 Jun 15. PMID: 15968136.

Salomé, M., Cotte, M., Baker, R., Barrett, R., Benseny-Cases, N., Berruyer, G., Bugnazet, D., Castillo-Michel, H., Cornu, C., Fayard, B., Gagliardini, E., Hino, R., Morse, J., Papillon, E., Pouyet, E., Rivard, C., Solé, V.A., Susini, J., Veronesi, G., 2013. The ID21 scanning X-ray microscope at ESRF. J. Phys. Conf. 425 (PART 18), 1–5. https://doi.org/10.1088/1742-6596/425/18/182004.

Senn, A.C., Kaegi, R., Hug, S.J., Hering, J.G., Mangold, S., Voegelin, A., 2015. Composition and structure of Fe(III)-precipitates formed by Fe(II) oxidation in water at near-neutral pH: interdependent effects of phosphate, silicate and Ca. Geochem. Cosmochim. Acta 162, 220–246. https://doi.org/10.1016/j.gca.2015.04.032.

Sharma, S.K., Petrusevski, B., Schippers, J.C., 2005. Biological iron removal from groundwater: a review. J. Water Supply Res. Technol. - Aqua 54 (4), 239–247. https://doi.org/10.2166/aqua.2005.0022.

Sharma, S., Petrusevski, B., Schippers, J.C., 2002. Characterisation of coated sand from iron removal plants. Water Sci. Technol. Water Supply 2 (2), 247–257. https://doi.org/10.2166/ws.2002.0070.

Tamura, H., Kawamura, S., Hagayama, M., 1980. Acceleration of the oxidation of Fe2+ ions by Fe(III)-oxyhydroxides. Corrosion Sci. 20 (8–9), 963–971. https://doi.org/10.1016/0010-938X(80)90077-3.

Tan, H., Zhang, G., Heaney, P.J., Webb, S.M., Burgos, W.D., 2010. Characterization of manganese oxide precipitates from Appalachian coal mine drainage treatment systems. Appl. Geochem. 25 (3), 389–399. https://doi.org/10.1016/j.apgeochem.2009.12.006.

Tebo, B.M., Bargar, J.R., Clement, B.G., Dick, G.J., Murray, K.J., Parker, D., Verity, R., Webb, S.M., 2004. Biogenic manganese oxides: properties and mechanisms of formation. Annu. Rev. Earth Planet Sci. 32 (1954), 287–328. https://doi.org/10.1146/annurev.earth.32.101802.120213. Goldberg.

Tekerlekopoulou, A.G., Pavlou, S., Vayenas, D.V., 2013. Removal of ammonium, iron and manganese from potable water in biofiltration units: a review. J. Chem. Technol. Biotechnol. 88 (5), 751–773. https://doi.org/10.1002/jctb.4031.

Tian, X., Zhang, R., Huang, T., Wen, G., 2019. The simultaneous removal of ammonium and manganese from surface water by MeOx: side effect of ammonium presence on manganese removal. J. Environ. Sci. (China) 77, 346–353. https://doi.org/10.1016/j.jes.2018.09.006.

Van Beek, C.G.E.M., Dusseldorp, J., Joris, K., Huysman, K., Leijssen, H., Schoonenberg Kegel, F., De Vet, W.W.J.M., Van De Wetering, S., Hofs, B., 2016. Contributions of homogeneous, heterogeneous and biological iron(II) oxidation in aeration and rapid sand filtration (RSF) in field sites. J. Water Supply Res. Technol. - Aqua 65 (3), 195–207. https://doi.org/10.2166/aqua.2015.059.

Van Kessel, M.A.H.J., Speth, D.R., Albertsen, M., Nielsen, P.H., Op Den Camp, H.J.M., Kartal, B., Jetten, M.S.M., Lücker, S., 2015. Complete nitrification by a single microorganism. Nature 528 (7583), 555–559. https://doi.org/10.1038/nature16459.

Vandenabeele, J., Vande Woestyne, M., Houwen, F., Germonpré, R., Vandesande, D., Verstraete, W., 1995. Role of autotrophic nitrifiers in biological manganese removal from groundwater containing manganese and ammonium. Microb. Ecol. 29 (1), 83–98. https://doi.org/10.1007/BF00217425.

Villalobos, M., Toner, B., Bargar, J., Sposito, G., 2003. Characterization of the manganese oxide produced by Pseudomonas putida strain MnB1. Geochem. Cosmochim. Acta 67 (14), 2649–2662. https://doi.org/10.1016/S0016-7037(03)00217-5.

Vries, D., Bertelkamp, C., Schoonenberg Kegel, F., Hofs, B., Dusseldorp, J., Bruins, J.H., de Vet, W., van den Akker, B., 2017. Iron and manganese removal: recent advances in modelling treatment efficiency by rapid sand filtration. Water Res. 109, 35–45. https://doi.org/10.1016/j.watres.2016.11.032.

Webb, S.M., Tebo, B.M., Bargar, J.R., 2005. Structural characterization of biogenic Mn oxides produced in seawater by the marine bacillus sp. strain SG-1. Am. Mineral. 90 (8–9), 1342–1357. https://doi.org/10.2138/am.2005.1669.

Yu, H., Leadbetter, J.R., 2020. Bacterial chemolithoautotrophy via manganese oxidation. Nature 583 (7816), 453–458. https://doi.org/10.1038/s41586-020-2468-5.

Zahoransky, T., Kaiser, K., Mikutta, C., 2022. High manganese redox variability and manganate predominance in temperate soil profiles as determined by X-ray absorption spectroscopy. Geochem. Cosmochim. Acta 338, 229–249. https://doi.org/10.1016/j.gca.2022.10.016.

Zhang, J., Lion, L.W., Nelson, Y.M., Shuler, M.L., Ghiorse, W.C., 2002. Kinetics of Mn(II) oxidation by Leptothrix discophora SS1. Geochem. Cosmochim. Acta 66 (5), 773–781. https://doi.org/10.1016/S0016-7037(01)00808-0.